THE ASTROPHYSICAL JOURNAL, 558:216–227, 2001 September 1

ELECTRODYNAMIC STRUCTURE OF AN OUTER GAP ACCELERATOR: LOCATION OF THE GAP AND THE GAMMA-RAY EMISSION FROM THE CRAB PULSAR

KOUICHI HIROTANI
National Astronomical Observatory, Osawa 2-21-1, Mitaka, Tokyo 181-8588, Japan; hirotani@hotaka.mtk.nao.ac.jp

AND

SHINPEI SHIBATA
Department of Physics, Yamagata University, Yamagata 990-8560, Japan; shibata@sci.kj.yamagata-u.ac.jp
Received 2000 November 27; accepted 2001 May 4

ABSTRACT

We investigate a stationary pair-production cascade in the outer magnetosphere of a spinning neutron star. The charge depletion due to global flows of charged particles causes a large electric field along the magnetic field lines. Migratory electrons and/or positrons are accelerated by this field to radiate curvature gamma rays, some of which collide with the X-rays to materialize as pairs in the gap. The replenished charges partially screen the electric field, which is self-consistently solved together with the distribution functions of particles and gamma rays. If no current is injected at either of the boundaries of the accelerator, the gap is located around the conventional null surface, where the local Goldreich-Julian charge density vanishes. However, we first find that the gap position shifts outward (or inward) when particles are injected at the inner (or outer) boundary. Applying the theory to the Crab pulsar, we demonstrate that the pulsed TeV flux does not exceed the observational upper limit for moderate infrared photon density and that the gap should be located near to or outside of the conventional null surface so that the observed spectrum of pulsed GeV fluxes may be emitted via a curvature process. Some implications of the existence of a solution for a super Goldreich-Julian current are discussed.

Subject headings: gamma rays: observations — gamma rays: theory — magnetic fields — pulsars: individual (Crab Pulsar) — X-rays: galaxies

1. INTRODUCTION

The EGRET experiment on the *Compton Gamma Ray Observatory* has detected pulsed signals from seven rotation-powered pulsars (e.g., for Crab, Nolan et al. 1993; Fierro et al. 1998). The modulation of the γ-ray light curves at GeV energies testifies to the production of γ-ray radiation in the pulsar magnetospheres either at the polar cap (Harding, Tademaru, & Esposito 1978; Daugherty & Harding 1982, 1996; Sturner, Dermer, & Michel 1995; Shibata, Miyazaki, & Takahara 1998) or at the vacuum gaps in the outer magnetosphere (Cheng, Ho, & Ruderman 1986a, 1986b; Chiang & Romani 1992, 1994; Romani & Yadigaroglu 1995; Romani 1996; Zhang & Cheng 1997; ZC97). Effective γ-ray production in a pulsar magnetosphere may be extended to the very high energy (VHE) region above 100 GeV as well; however, the predictions of fluxes by the current models of γ-ray pulsars are not sufficiently conclusive. Whether or not the spectra of γ-ray pulsars continue up to the VHE region is a question that remains one of the interesting issues of high-energy astrophysics.

In the VHE region, positive detections of radiation at a high confidence level have been reported from the direction of the Crab pulsar (Nel et al. 1993). However, as for *pulsed* TeV radiation, only the upper limits, as a rule, have been obtained (Akerlof et al. 1993; Borione et al. 1997; Srinivasan et al. 1997; Yoshikoshi et al. 1997; Sako et al. 2000). If the VHE emission originates in the pulsar magnetosphere, a significant fraction of it can be expected to show pulsation. Therefore, the lack of *pulsed* TeV emissions provides a severe constraint on the modeling of particle acceleration zones in a pulsar magnetosphere.

In fact, in the picture provided by Cheng et al. (1986a, 1986b), the magnetosphere should be optically thick for pair production in order to reduce the TeV flux to an unobserved level by absorption. This in turn requires very high luminosities of infrared photons. However, the required IR fluxes are generally orders of magnitude larger than the observed values (Usov 1994). We are therefore motivated by the need to contrive an outer gap model that produces less TeV emission with a moderate infrared luminosity.

High-energy emission from a pulsar magnetosphere, in fact, crucially depends on the acceleration electric field, $E_{\parallel}$, along the magnetic field lines. It was Hirotani & Shibata (1999a, 1999b, 1999c; hereafter Papers I, II, III) and Hirotani (2000b, hereafter Paper VI) who first considered the spatial distribution of $E_{\parallel}$ together with particle and γ-ray distribution functions. By solving these Vlasov equations, they demonstrated that a stationary gap is formed around the conventional null surface at which the local Goldreich-Julian charge density,

$$\rho_{\rm GJ} = -\frac{\Omega B_z}{2\pi c}\,, \tag{1}$$

vanishes, where B_z is the component of the magnetic field along the rotation axis, Ω the angular frequency of the neutron star, and c the speed of light. Equation (1) is valid unless the gap is located close to the light cylinder, of which distance from the rotation axis is given by $\varpi_{\rm LC} = c/\Omega$. The electrodynamic model developed in this paper is basically the same as that of Paper VI. However, we find an interesting behavior of the gap position by relaxing the boundary conditions to allow electric current injection through the inner or the outer boundaries of the gap.

Subsequently, Hirotani (2000a, hereafter Paper IV; 2001, Paper V) considered the "gap closure condition" so that a gap may maintain a stationary pair-production cascade. In this paper, this closure condition is generalized into the case in which the currents are injected through the boundaries.

In the next two sections, we describe the physical processes of pair-production cascade and the resultant γ-ray emission. We then apply the theory to the Crab pulsar and present the expected γ-ray spectra in § 5. In the final section, we discuss the possibility of a gap formation for a super Goldreich-Julian current.

2. ANALYTIC EXAMINATION OF THE GAP POSITION

Let us first consider the gap position analytically when there is a current injection into the gap. We consider the particle continuity equations in § 2.1 and the γ-ray Boltzmann equations in § 2.2.

2.1. *Particle Continuity Equations*

Under the monoenergetic approximation, we simply assume that the electrostatic and the curvature–radiation-reaction forces cancel each other in the Boltzmann equations of particles. Then the spatial number density of the outwardly and inwardly propagating particles, $N_+(s)$ and $N_-(s)$, at distance s from the neutron-star surface along the last-open field line, obey the following continuity equations:

$$\frac{\partial N_\pm}{\partial t} + \boldsymbol{v}\cdot\frac{\partial N_\pm}{\partial \boldsymbol{x}} = Q(\boldsymbol{x})\,, \tag{2}$$

where

$$Q(\boldsymbol{x}) \equiv \frac{1}{c}\int_0^\infty d\epsilon_\gamma[\eta_{\rm p+}\,G_+ + \eta_{\rm p-}\,G_-]\;; \tag{3}$$

$G_+(\boldsymbol{x}, \epsilon_\gamma)$ and $G_-(\boldsymbol{x}, \epsilon_\gamma)$ refer to the distribution functions of outwardly and inwardly propagating γ-ray photons, respectively, having energy $m_{\rm e}c^2\epsilon_\gamma$. The pair-production rate for an outwardly propagating (or inwardly propagating) γ-ray photon to materialize as a pair per unit time is expressed by $\eta_{\rm p+}$ (or $\eta_{\rm p-}$). For charge definiteness, we consider that a positive electric field arises in the gap. In this case, N_+ (or N_-) represents the number densities of positrons (or electrons).

The particle velocity at position (r, θ) becomes (eq. [21] in Paper VI)

$$\boldsymbol{v} = \boldsymbol{v}_{\rm p} + \left(r\Omega\,\sin\,\theta + \kappa B_\phi - cE_\parallel\,\frac{B_\phi}{B^2}\right)\boldsymbol{e}_\phi\,, \tag{4}$$

where κ is a constant and $\boldsymbol{e}_\phi$ refers to the azimuthal unit vector. In the parentheses, the term $r\Omega\,\sin\,\theta$ is caused by corotation, while κB_ϕ is caused by magnetic bending. Since $E_\parallel$ arises in the gap, the corresponding drift velocity appears as $-cE_\parallel\,B_\phi/B^2$. Unless the gap is located close to the light cylinder, we can neglect the terms containing B_ϕ as a first-order approximation. We thus have

$$\boldsymbol{v} \approx \boldsymbol{v}_{\rm p} + r\Omega\,\sin\,\theta\boldsymbol{e}_\phi\,. \tag{5}$$

Imposing a stationarity condition

$$[\partial_t + (r\Omega\,\sin\,\theta)\partial_\phi]N_\pm = 0\,, \tag{6}$$

reminding that the projected velocity on the poloidal plane is $\boldsymbol{v}_{\rm p} = c\,\cos\,\Phi\boldsymbol{B}_{\rm p}/B_{\rm p}$, and utilizing ${\rm div}\boldsymbol{B}_{\rm p} \approx {\rm div}\boldsymbol{B} = 0$, we obtain

$$\pm B\,\frac{\partial}{\partial s}\left(\frac{N_\pm}{B}\right) = \frac{1}{c\,\cos\,\Phi}\int_0^\infty d\epsilon_\gamma[\eta_{\rm p+}\,G_+ + \eta_{\rm p-}\,G_-]\,, \tag{7}$$

where Φ refers to the projection angle of the particle three-dimensional motion onto the poloidal plane. It is defined by $\Phi = \arcsin\,(r_{\rm cnt}\Omega\,\sin\,\theta/c)$, where $r_{\rm cnt}$ is the distance of the gap center from the star center. The pair-production rate per unit of time by a single γ-ray photon, $\eta_{\rm p\pm}$, is defined as

$$\eta_{\rm p\pm}(\epsilon_\gamma) = (1-\mu_{\rm c})c\int_{\epsilon_{\rm th}}^\infty d\epsilon_{\rm x}\,\frac{dN_{\rm x}}{d\epsilon_{\rm x}}\,\sigma_{\rm p}(\epsilon_\gamma, \epsilon_{\rm x}, \mu_{\rm c})\,, \tag{8}$$

where $\sigma_{\rm p}$ is the pair-production cross section and $\cos^{-1}\,\mu_{\rm c}$ refers to the collision angle between the γ-rays and the X-rays (see Paper VI for more details about eq. [8]); $\epsilon_{\rm th} \equiv 2/[(1-\mu_{\rm c})\epsilon_\gamma]$. The adopted value of $\mu_{\rm c}$ will be detailed in § 5.2. The quantity $\epsilon_{\rm x}$ refers to the X-ray energy in the unit of $m_{\rm e}c^2$.

Although $\Phi \neq 0$ is adopted after § 3.1, in this section we simply neglect the projection effect of the poloidal velocity and put $\Phi = 0$. Then equation (7) gives

$$\pm B\,\frac{d}{ds}\left(\frac{N_\pm}{B}\right) = \frac{1}{\lambda_{\rm p}}\int_0^\infty d\epsilon_\gamma(G_+ + G_-)\,, \tag{9}$$

where $G_+(s, \epsilon_\gamma)$ and $G_-(s, \epsilon_\gamma)$ refer to the distribution functions of the outwardly and inwardly propagating γ-rays; the mean free path $\lambda_{\rm p}$ is defined by

$$\lambda_{\rm p} \equiv \frac{1}{c}\,\frac{\int_0^\infty \eta_{\rm p+}\,G_+\,d\epsilon_\gamma}{\int_0^\infty G_+\,d\epsilon_\gamma}\,. \tag{10}$$

Since $W \ll \varpi_{\rm LC}$ is justified for the Crab pulsar (Paper V), we regard $\lambda_{\rm p}$ to be constant in the gap in this section.

2.2. *Boltzmann Equations for Gamma Rays*

Unlike the charged particles, γ-rays do not propagate along the magnetic field line at each point because they preserve the directional information where they were emitted. However, to avoid complications, we simply assume that the outwardly (or inwardly) propagating γ-rays dilate (or constrict) at the same rate with the magnetic field. This assumption gives a good estimate when $W \ll \varpi_{\rm LC}$ holds. We then obtain (Paper VI)

$$\pm B\,\frac{\partial}{\partial s}\left(\frac{G_\pm}{B}\right) = -\,\frac{\eta_{\rm p\pm}}{c\,\cos\,\Phi}\,G_\pm + \frac{\eta_{\rm c}}{c\,\cos\,\Phi}\,N_\pm\,, \tag{11}$$

where (e.g., Rybicki & Lightman 1979)

$$\eta_{\rm c} \equiv \frac{\sqrt{3}e^2\Gamma}{hR_{\rm C}}\,\frac{1}{\epsilon_\gamma}\,F\!\left(\frac{\epsilon_\gamma}{\epsilon_{\rm c}}\right), \tag{12}$$

$$\epsilon_{\rm c} \equiv \frac{1}{m_{\rm e}c^2}\,\frac{3}{4\pi}\,\frac{hc\Gamma^3}{R_{\rm C}}\,, \tag{13}$$

$$F(s) \equiv s\int_x^\infty K_{5/3}(t)dt\;; \tag{14}$$

$R_{\rm C}$ is the curvature radius of the magnetic field lines and $K_{5/3}$ is the modified Bessel function of 5/3 order. The effect of the broad spectrum of curvature γ-rays is represented by the factor $F(\epsilon_\gamma/\epsilon_{\rm c})$ in equation (12).

Noting that the absorption caused by pair production is negligible compared with the curvature emission term on the right-hand side of equation (11), and putting $\Phi = 0$

again, we obtain

$$\pm\frac{\partial}{\partial s}\left[\frac{1}{B}\,G_{\pm}(s,\,\epsilon_\gamma)\right]=\frac{\eta_c(\epsilon_\gamma)}{c}\,\frac{N_{\pm}(s)}{B}\,. \tag{15}$$

Integrating equation (15) over ϵ_γ, and combining with equation (9), we obtain

$$\pm\frac{d^2}{ds^2}\left(\frac{N_{\pm}}{B}\right)=\frac{1}{\lambda_p c}\,\frac{N_+-N_-}{B}\int_{\beta_0}^{\beta_N}\eta_c(\epsilon_\gamma)d\epsilon_\gamma\,, \tag{16}$$

where β_N is the upper cutoff dimensionless γ-ray energy. In the present paper, we set $\beta_N=\beta_9=10^{5.5}$ (see § 3.1).

One combination of the two independent equations that constitute(16) yields the conserved current per magnetic flux tube,

$$\frac{\Omega}{2\pi}\,j_{\rm tot}=ce\,\frac{N_+(s)+N_-(s)}{B(s)}\,. \tag{17}$$

If $j_{\rm tot}=1.0$, the conserved current density becomes its Goldreich-Julian value. Another combination of the equations that constitute (16) gives

$$\frac{d^2}{ds^2}\left(\frac{N_+-N_-}{B}\right)=\frac{4N_\gamma}{\lambda_p}\,\frac{N_+-N_-}{B}\,, \tag{18}$$

where

$$N_\gamma\equiv\frac{W/2}{c}\int_{\beta_0}^{\beta_N}\eta_c(\epsilon_\gamma)d\epsilon_\gamma \tag{19}$$

refers to the expectation value of the number of γ-rays emitted by a single particle that runs a typical length $W/2$ in the gap.

In a stationary gap, the pair-production optical depth, W/λ_p, must equal the expectation value for a γ-ray to materialize with the gap, $N_\gamma^{-1}(j_{\rm gap}/j_{\rm tot})$. We thus obtain the following condition:

$$W=\frac{\lambda_p}{N_\gamma}\,\frac{j_{\rm gap}}{j_{\rm tot}}\,, \tag{20}$$

which is automatically satisfied by the stationary Vlasov equations. Here, the dimensionless current density, $j_{\rm gap}$, created in the gap is defined by

$$\begin{aligned}\frac{\Omega}{2\pi ce}\,j_{\rm gap}&\equiv\frac{N_+(s_2)}{B(s_2)}-\frac{N_+(s_1)}{B(s_1)}\\&=\frac{N_-(s_1)}{B(s_1)}-\frac{N_-(s_2)}{B(s_2)}\,,\end{aligned} \tag{21}$$

where s_1 and s_2 designate the position of the inner and the outer boundaries, respectively. That is, $W=s_2-s_1$. Equation (20) corresponds to a generalized version of the gap closure condition considered in Papers IV and V (e.g., eq. [30] in Paper V), in which $j_1=j_2=0$ and, hence, $j_{\rm gap}=j_{\rm tot}$ was assumed. When there is a current injection (i.e., when j_1 or j_2 is nonvanishing), not only the produced particles in the gap but also the injected particles contribute to the γ-ray emission. Therefore, the gap width is adjusted smaller compared with the $j_1=j_2=0$ case by the factor $j_{\rm gap}/j_{\rm tot}$. Utilizing condition (20), we can rewrite equation (18) into the form

$$\frac{d^2}{ds^2}\left(\frac{N_+-N_-}{B}\right)=4\,\frac{j_{\rm tot}}{j_{\rm gap}}\,\frac{1}{W}\,\frac{N_+-N_-}{B}\,. \tag{22}$$

To solve the differential equation (22), we impose the following two boundary conditions:

$$ce\,\frac{N_+(s_1)}{B(s_1)}=\frac{\Omega}{2\pi}\,j_1\,, \tag{23}$$

$$ce\,\frac{N_-(s_2)}{B(s_2)}=\frac{\Omega}{2\pi}\,j_2\,. \tag{24}$$

With the aid of equation (21), these two boundary conditions give

$$\frac{N_+-N_-}{B}=-\frac{\Omega}{2\pi}\,(j_{\rm gap}-j_1+j_2) \tag{25}$$

at $s=s_1$, and

$$\frac{N_+-N_-}{B}=\frac{\Omega}{2\pi}\,(j_{\rm gap}+j_1-j_2) \tag{26}$$

at $s=s_2$. It follows from equation (22)

$$\begin{aligned}\frac{N_+-N_-}{B}=\frac{\Omega}{2\pi ce}\Bigg[&j_{\rm gap}\,\frac{\sinh\left(\sqrt{(j_{\rm tot}/j_{\rm gap})}\,(s-s_{\rm cnt}/W/2)\right)}{\sinh\left(\sqrt{(j_{\rm tot}/j_{\rm gap})}\right)}\Bigg]\\&+\Bigg[(j_1-j_2)\,\frac{\cosh\left(\sqrt{(j_{\rm tot}/j_{\rm gap})}\,(s-s_{\rm cnt}/W/2)\right)}{\cosh\left(\sqrt{(j_{\rm tot}/j_{\rm gap})}\right)}\Bigg],\end{aligned} \tag{27}$$

where the gap center position is defined by

$$s_{\rm cnt}\equiv\frac{s_2-s_1}{2}\,. \tag{28}$$

2.3. *Poisson Equation*

The real charge density $e(N_+-N_-)$, which is given by equation (27), appears in the Poisson equation for the noncorotational potential Ψ. Neglecting relativistic effects, and assuming that typical transfield thickness of the gap, $D_\perp$, is greater than or comparable with W, we can reduce the Poisson equation into the one-dimensional form (Paper VI; see also § 2 in Michel 1974)

$$-\nabla^2\Psi=4\pi\left[e(N_+-N_-)+\frac{\Omega B_z}{2\pi c}\right], \tag{29}$$

where e designates the magnitude of the charge on an electron. Substituting equation (27) into (29), we obtain

$$\begin{aligned}-\nabla^2\Psi=\frac{2B\Omega}{c}\Bigg[&j_{\rm gap}\,f_{\rm odd}\left(\frac{s-s_{\rm cnt}}{W/2}\right)\\&+(j_1-j_2)f_{\rm even}\left(\frac{s-s_{\rm cnt}}{W/2}\right)+\frac{B_z}{B}\Bigg],\end{aligned} \tag{30}$$

where

$$f_{\rm odd}(x)\equiv\frac{\sinh\left(\sqrt{(j_{\rm tot}/j_{\rm gap})}\,x\right)}{\sinh\left(\sqrt{(j_{\rm tot}/j_{\rm gap})}\right)} \tag{31}$$

and

$$f_{\rm even}(x) \equiv \frac{\cosh\left(\sqrt{(j_{\rm tot}/j_{\rm gap})}\,x\right)}{\cosh\left(\sqrt{(j_{\rm tot}/j_{\rm gap})}\right)} . \tag{32}$$

There are essentially three assumptions that are used to derive equations (30), (31), and (32): the radiation-reaction forces exactly cancel with the electrostatic force in the particles' Boltzmann equations; $\eta_{\rm p+}(\epsilon_\gamma) = \eta_{\rm p-}(\epsilon_\gamma)$, which may be justified for a power-law, magnetospheric X-ray component; and the Poisson equation is analyzed one-dimensionally along the magnetic field line.

2.4. *Generalization of the Null Surface*

To examine the Poisson equation (30) analytically, we assume that the transfield thickness of the gap is greater than W and replace $\nabla^2\Psi$ with $d^2\Psi/ds^2$. Furthermore, we neglect the current created in the gap and simply set $j_{\rm gap} = 0$.

First, consider the case when a current injects from neither of the boundaries, that is, $j_1 = j_2 = 0$. It follows that the derivative of the acceleration field (i.e., $-d^2\Psi/ds^2$) vanishes at the conventional null surface where B_z vanishes. We may notice that $-d^2\Psi/ds^2$ is positive at the inner part of the gap and changes its sign near the gap center ($s = s_{\rm cnt}$) to become negative at the outer part of the gap. Therefore, we can conclude that the gap is located (or centers) around the conventional null surface, if there is no current injection from outside.

Second, consider the case when a current is injected at the inner boundary (at $s = s_1$) and $j_1 - j_2 > 0$ holds. Since the function $f_{\rm even}$ is positive at arbitrary s, the gap center is located at a place where B_z is negative, that is, outside of the conventional null surface. In particular, when $j_1 - j_2 \sim 1$ holds, $-d^2\Psi/ds^2$ vanishes at the place where $B_z \sim -B$. In a vacuum, static dipole field, $B_z \sim -B$ is realized along the last-open field line at the light cylinder. Therefore, the gap is expected to shift toward the light cylinder, if the injected current density at the inner boundary approaches the Goldreich-Julian value. We may notice here that $f_{\rm even}$ is less than unity because $|s - s_{\rm cnt}|$ does not exceed $W/2$.

Third and finally, consider the case when $j_1 - j_2 \sim -1$ holds. In this case, $-d^2\Psi/ds^2$ vanishes at the place where $B_z \sim B$. Therefore, the gap is expected to be located close to the star surface, if a Goldreich-Julian current density is injected at the outer boundary. In what follows, we will examine more accurately these predictions on the gap position versus current injection by solving the Vlasov equations (7), (11), and (30) numerically.

3. BASIC EQUATIONS AND BOUNDARY CONDITIONS

In this paper, we assume that the transfield thickness, $D_\perp$, of the gap is much greater than W and neglect the transfield derivatives in the Poisson equation (29). We consider that this one-dimensional analysis could be justified because $D_\perp \sim 6W$ is required so that the predicted GeV flux may be consistent with the EGRET observations (§ 5.3.1). We rewrite the Vlasov equations into the suitable forms for numerical analysis in § 3.1 and impose boundary conditions in § 3.2.

3.1. *One-dimensional Vlasov Equations*

As will be shown at the end of this section, it is convenient to introduce the typical Debye scale length $c/\omega_{\rm p}$,

$$\omega_{\rm p} = \sqrt{\frac{4\pi e^2}{m_{\rm e}}\frac{\Omega B_{\rm cnt}}{2\pi ce}} , \tag{33}$$

where $B_{\rm cnt}$ represents the magnetic field strength at the gap center. The dimensionless coordinate variable then becomes

$$\xi \equiv (\omega_{\rm p}/c)s . \tag{34}$$

By using such dimensionless quantities, we can rewrite the Poisson equation into

$$E_\parallel = -\frac{d\psi}{d\xi} , \tag{35}$$

$$\frac{dE_\parallel}{d\xi} = \frac{B(\xi)}{B_{\rm cnt}}\left[n_+(\xi) - n_-(\xi)\right] + \frac{B_z(\xi)}{B_{\rm cnt}} , \tag{36}$$

where $\psi(\xi) \equiv e\Psi(s)/(m_{\rm e}c^2)$; the particle densities per unit flux tube are defined by

$$n_\pm(\xi) \equiv \frac{2\pi ce}{\Omega}\frac{N_\pm}{B} . \tag{37}$$

We evaluate B_z/B at each point along the last-open field line by using the Newtonian dipole field.

Let us introduce the following dimensionless γ-ray densities in the dimensionless energy interval between β_{i-1} and β_i:

$$g^i_\pm(\xi) \equiv \frac{2\pi ce}{\Omega B_{\rm cnt}}\int_{\beta_{i-1}}^{\beta_i} d\epsilon_\gamma\, G_\pm(s, \epsilon_\gamma) . \tag{38}$$

In this paper, we set $\beta_0 = 10^2$, which corresponds to the lowest γ-ray energy, 51.1 MeV. We divide the γ-ray spectra into nine energy bins and put $\beta_1 = 10^{2.5}$, $\beta_2 = 10^3$, $\beta_3 = 10^{3.5}$, $\beta_4 = 10^4$, $\beta_5 = 10^{4.5}$, $\beta_6 = 10^{4.75}$, and $\beta_7 = 10^5$. $\beta_8 = 10^{5.25}$, and $\beta_9 = 10^{5.5}$.

We can now rewrite the continuity equation (7) of particles into

$$\frac{dn_\pm}{d\xi} = \pm\frac{B_{\rm cnt}}{B\cos\Phi}\sum_{i=1}^{9}\left[\eta_{\rm p+}\,{}^ig^i_+(\xi) + \eta_{\rm p-}\,{}^ig^i_-(\xi)\right] , \tag{39}$$

where the magnetic field strength, B, is evaluated at each ξ. The dimensionless redistribution functions $\eta^i_{\rm p\pm}$ are evaluated at the central energy in each bin as

$$\eta^i_{\rm p\pm} \equiv \frac{1}{\omega_{\rm p}}\,\eta_{\rm p\pm}\left(\frac{\beta_{\rm i-1} + \beta_{\rm i}}{2}\right) . \tag{40}$$

A combination of the equations in (39) gives the current conservation law,

$$j_{\rm tot} \equiv n_+(\xi) + n_-(\xi) = \text{constant for } \xi , \tag{41}$$

which is equivalent with equation (17).

The Boltzmann equations in (11) for the γ-rays are integrated over ϵ_γ between dimensionless energies $\beta_{\rm i-1}$ and $\beta_{\rm i}$ to become

$$\frac{d}{d\xi}\,g^i_\pm = \frac{d}{d\xi}(\ln B) \mp \frac{\eta^i_{\rm p\pm}}{\cos\Phi}\,g^i_\pm \pm \frac{\eta^i_{\rm c}\,B(\xi)}{B_{\rm cnt}\cos\Phi}\,n_\pm , \tag{42}$$

where $i = 1, 2, \ldots, m\,(m = 9)$ and

$$\eta^i_{\rm c} \equiv \frac{\sqrt{3}e^2\Gamma}{\omega_{\rm p}hR_{\rm c}}\int_{\beta_{i-1}/\epsilon_{\rm c}}^{\beta_i/\epsilon_{\rm c}} ds\int_s^\infty K_{5/3}(t)dt \tag{43}$$

is dimensionless.

Equating the electric force $e|d\Psi/dx|$ and the radiation reaction force, we obtain the saturated Lorentz factor at each point as

$$\Gamma_{\rm sat} = \left(\frac{3R_{\rm c}^{\ 2}}{2e} \left| \frac{d\Psi}{ds} \right| + 1 \right)^{1/4} ; \tag{44}$$

we compute the curvature radius $R_{\rm c}$ at each point for a Newtonian dipole magnetic field. Since the maximum of $|d\Psi/dx|$ and the potential drop are roughly proportional to W^2 and W^3, respectively (Paper V), the particles become unsaturated for very small W. To avoid an overestimation of the Lorentz factor in such cases, we compute Γ by

$$\frac{1}{\Gamma} = \sqrt{\frac{1}{\Gamma_{\rm sat}^{\ 2}} + \frac{1}{\psi^2(\xi_2)}} , \tag{45}$$

where $\psi(\xi_2)$ represents the maximum attainable Lorentz factor.

3.2. *Boundary Conditions*

We now consider the boundary conditions to solve the Vlasov equations (35), (36), (39), and (42). At the *inner* (starward) boundary ($\xi = \xi_1$), we impose (Paper VI)

$$E_{\parallel}(\xi_1) = 0 , \tag{46}$$

$$\psi(\xi_1) = 0 , \tag{47}$$

$$g^i_{+}(\xi_1) = 0 \quad (i = 1, 2, \ldots, 9) . \tag{48}$$

It is noteworthy that condition (46) is consistent with the stability condition at the plasma-vacuum interface if the electrically supported magnetospheric plasma is completely charge-separated, i.e., if the plasma cloud at $\xi < \xi_1$ is composed of electrons alone (Krause-Polstorff & Michel 1985a, 1985b; Michel 1991). We assume that the Goldreich-Julian plasma gap boundary is stable with $E_{\parallel} = 0$ on the boundary, $\xi = \xi_1$.

Since positrons may flow into the gap at $\xi = \xi_1$ as a part of the global current pattern in the magnetosphere, we denote the positronic current per unit flux tube at $\xi = \xi_1$ as

$$n_{+}(\xi_1) = j_1 , \tag{49}$$

which yields (eq. [41])

$$n_{-}(\xi_1) = j_{\rm tot} - j_1 . \tag{50}$$

At the *outer* boundary ($\xi = \xi_2$), we impose

$$E_{\parallel}(\xi_2) = 0 , \tag{51}$$

$$g^i_{-}(\xi_2) = 0 \quad (i = 1, 2, \ldots, 9) , \tag{52}$$

$$n_{-}(\xi_2) = j_2 . \tag{53}$$

Conditions (49) and (53) are equivalent with (23) and (24).

The current density created in the gap per unit flux tube can be expressed as

$$j_{\rm gap} = j_{\rm tot} - j_1 - j_2 . \tag{54}$$

This equation is, of course, consistent with equation (21). We adopt $j_{\rm gap}$, j_1, and j_2 as the free parameters.

We have a total of 24 boundary conditions (46)–(53) for 22 unknown functions Ψ, $E_{\parallel}$, $n_{\pm}$, $g^i_{\pm}$ ($i = 1, 2, \ldots, 9$). Thus, two extra boundary conditions must be compensated by making the positions of the boundaries ξ_1 and ξ_2 be free. The two free boundaries appear because $E_{\parallel} = 0$ is imposed at *both* the boundaries and because $j_{\rm gap}$ is externally imposed. In other words, the gap boundaries (ξ_1 and ξ_2) shift, if j_1 and/or j_2 varies.

Let us briefly comment on the convenience of the introduction of the dimensionless coordinates and variables. It follows from the Vlasov equations (35), (36), (39), and (42) that the solutions ξ, ψ, $E_{\parallel}$, $n_{\pm}$, and $g^i_{\pm}$ are unchanged if B, $\eta^i_{\rm p\pm}$, and $\eta^i_{\rm c}$ are invariant. Consider the case when the normalization of $dN_{\rm x}/d\epsilon_{\rm x}$ is doubled. In this case, equations (8) and (40) show that $\eta^i_{\rm p}$ is invariant if we also double $\omega_{\rm p}$. Note that $\epsilon_{\rm c}$ in equation (43) is proportional to $\omega_{\rm p}^{3/4} R_{\rm c}^{1/2}$ (eq. [13]), where $\Gamma \sim \Gamma_{\rm sat} \propto R_{\rm c}^{1/2} |d\Psi/ds|^{1/4}$ is used. It follows that $\epsilon_{\rm c}$ is also invariant if we increase $R_{\rm c}$ by $2^{-3/2}$ times. It should be noted that $\eta^i_{\rm c}$ (eq. [43]) is invariant by this change of parameters. On these grounds, we can reduce one degree of freedom in the free parameters.

4. PREDICTED GAMMA-RAY FLUX

In this section, we detail the method for computing the νF_ν spectrum in GeV energies in § 4.1 and in TeV energies in § 4.2.

4.1. *GeV Spectra*

The GeV spectra of outwardly and inwardly propagating γ-rays are obtained from $g^i_{+}(\xi_2)$ and $g^i_{-}(\xi_1)$. At position ξ, the γ-ray emission rate becomes

$$\gamma - \text{ray flux} = A_{\rm cr}(\xi)\, c\, \frac{\Omega B_{\rm cnt}}{2\pi ce}\, g^i_{\pm}(\xi)\ {\rm s}^{-1} , \tag{55}$$

where $A_{\rm cr}$ refers to the cross section of the gap at ξ. Multiplying the mean γ-ray energy $\sqrt{\beta_{\rm i}\beta_{\rm i-1}}\, m_{\rm e} c^2$, on equation (55), dividing it by $\Delta\Omega_{\rm GeV} d^2$, and further dividing by the frequency interval $m_{\rm e} c^2(\beta_{\rm i} - \beta_{\rm i-1})/h$, we obtain the flux density, F_ν; here, $\Delta\Omega_{\rm GeV}$ is the emission solid angle, and h is the Planck constant. We thus obtain the GeV flux

$$\nu F_\nu = \frac{\beta_{\rm i}\beta_{\rm i-1}}{\beta_{\rm i} - \beta_{\rm i-1}}\, m_{\rm e} c^2\, \frac{\Omega B_{\rm cnt}}{2\pi e}\, \frac{A_{\rm cr} g^{\rm i}_{\pm}}{\Delta\Omega_{\rm GeV}\ d^2} . \tag{56}$$

To compute the γ-ray flux emitted outwardly (or inwardly) from the gap, we adopt the plus (or the minus) sign in $g_{\pm}$ and evaluate $A_{\rm cr} g_{+}$ at $\xi = \xi_2$ (or ξ_1). As will be shown in § 5.3, $W \ll \varpi_{\rm LC}$ holds for the Crab pulsar. We thus simply apply the same cross section for both the outwardly and inwardly emitted γ-rays and put $A_{\rm cr} = D_{\perp}^2$, where $D_{\perp}$ should be greater than or at least comparable with W for the one-dimensional approximation of the Poisson equation (29) to be justified.

It is noteworthy that the particles lose most of their energy in the gap if $l_{\rm acc} \ll W$ holds, where $l_{\rm acc}$ refers to the length scale for particles to be accelerated to the saturated Lorentz factor (eq. [44]). That is, we can neglect the primary luminosity emitted by the particles running *outside* of the gap, compared with that emitted by the particles running *inside* of the gap, if $l_{\rm acc} \ll W$. Since the monoenergetic approximation of the particle motion (§ 2.1) is justified when $l_{\rm acc} \ll W$, the neglect of GeV emission by the particles running outside of the gap is consistent with the monoenergetic approximation. We thus compute the GeV luminosity from the solved γ-ray distribution functions $g^i_{+}(\xi_2)$ and $g^i_{-}(\xi_1)$.

4.2. *TeV Spectra*

Once the electrodynamic structure of the gap is solved, we can further compute the upscattered γ-ray flux emitted

from the whole accelerator, if additionally given the infrared photon field. This treatment is justified unless the upscattered, TeV luminosity exceeds the curvature-radiated, GeV one.

If an electron or a positron is migrating with Lorentz factor $\Gamma \gg 1$ in an isotropic photon field, it upscatters the soft photons to produce the following number spectrum of γ-rays (Blumenthal & Gould 1970):

$$\frac{dN}{dtd\epsilon_\gamma} = \frac{3}{4}\sigma_T \frac{c}{\Gamma^2}\frac{dN_{IR}}{d\epsilon_{IR}}\frac{d\epsilon_{IR}}{\epsilon_{IR}} \times \left[2q\ln q + (1+2q)(1-q) + \frac{(Qq)^2(1-q)}{2(1+Qq)}\right], \quad (57)$$

where $Q \equiv 4\epsilon_{IR}\Gamma$, $q \equiv \epsilon_\gamma/Q(\Gamma - \epsilon_\gamma)$, $dN_{IR}/d\epsilon_{IR}$ refers to the IR photon density per unit dimensionless energy interval between ϵ_{IR} and $\epsilon_{IR} + d\epsilon_{IR}$, σ_T is the Thomson cross section; ϵ_{IR} and ϵ_γ are the energies of the IR and the upscattered photons in units of $m_e c^2$. Equation (57) is valid if the resonance effects are negligible, that is, $B \ll B_{crit} = 4.4 \times 10^{13}$ G. This inequality is satisfied except for the polar cap. The flux density of the upscattered photons becomes

$$F_\nu = \frac{N_e}{\Delta\Omega_{TeV}\, d^2}\cdot h\epsilon_\gamma \int_{\epsilon_{IR,min}}^{\epsilon_{IR,max}} \frac{dN}{dt\, d\epsilon_\gamma\, d\epsilon_{IR}}\, d\epsilon_{IR}\,, \quad (58)$$

where $\Delta\Omega_{TeV}$ refers to the emission solid angle of the upscattered photons. In this paper, we estimate N_e with

$$N_e = (j_{gap} + j_1)\frac{\Omega B_{cnt}}{2\pi ce} W D_\perp{}^2 \quad (59)$$

to compute the outwardly propagating TeV flux, which are emitted by outwardly propagating particles (i.e., positrons) and with

$$N_e = (j_{gap} + j_2)\frac{\Omega B_{cnt}}{2\pi ce} W D_\perp{}^2 \quad (60)$$

to compute the inwardly propagating TeV flux, which are emitted by inwardly propagating particles (i.e., electrons).

Multiplying the γ-ray frequency $\epsilon_\gamma m_e c^2/h$ on the F_ν flux density (eq. [58]), we obtain the upscattered flux

$$\nu F_\nu = (j_{gap} + j_a) m_e c^2 \frac{\Omega B_{cnt}}{2\pi e}\frac{A_{cr}}{\Delta\Omega_{TeV} d^2}\epsilon_\gamma{}^2 \times W\int_{\epsilon_{IR,min}}^{\epsilon_{IR,max}} \frac{dN}{cdt\, d\epsilon_\gamma\, d\epsilon_{IR}}\, d\epsilon_{IR}\,, \quad (61)$$

where $j_a = j_1$ (or j_2) for outwardly (or inwardly) emitted γ-rays. As the emission solid angles, we assume

$$\Delta\Omega_{GeV} = \Delta\Omega_{TeV} = \frac{2\pi W}{\varpi_{LC}} \quad (62)$$

in this paper.

We also consider the extrinsic absorption of the TeV photons outside of the gap. For a homogeneous and isotropic IR field, the optical depth becomes

$$\tau(\epsilon_\gamma) = \frac{\varpi_{LC}}{2}\int_{\epsilon_{IR,min}}^{\epsilon_{IR,max}} \frac{dN_{IR}}{d\epsilon_{IR}}\sigma_p(\epsilon_{IR}, \epsilon_\gamma, \mu_c) d\epsilon_{IR}\,, \quad (63)$$

where the path length is assumed to be $\varpi_{LC}/2$. We apply the same path length for all the cases considered so that the extrinsic absorption may work equally.

5. APPLICATION TO THE CRAB PULSAR

5.1. *Input Infrared Field*

Consider the case when the IR spectrum is homogeneous and expressed by a single power law,

$$\frac{dN_{IR}}{d\epsilon_{IR}} = N_0\,\epsilon_{IR}^{\alpha}\,, \quad (64)$$

where N_0 and α are spatially constant. For an isotropic field, the specific intensity becomes

$$I_\nu = \frac{c}{4\pi} hN_0\,\epsilon_{IR}^{\alpha+1}\,. \quad (65)$$

Assuming that this uniform sphere has radius ϖ_{LC}, we obtain the following flux density at distance d:

$$F_\nu = \frac{c}{4}\left(\frac{\varpi_{LC}}{d}\right)^2 hN_0\,\epsilon_{IR}{}^{\alpha+1} = 4.5\times 10^{-20}\Omega_2{}^{-2}\left(\frac{d}{\mathrm{kpc}}\right)^{-2} N_0\,\epsilon_{IR}{}^{\alpha+1}\mathrm{Jy}\,. \quad (66)$$

As the lower and upper cutoff IR photon energies, we adopt $\epsilon_{IR,\,min} = 10^{-8}$ and $\epsilon_{IR,\,max} = 10^{-6}$, where $\epsilon_{IR,\,min} < \epsilon_{IR} < \epsilon_{IR,\,max}$.

Because the pulsed flux around eV energies is difficult to observe, we consider the following two cases for the set of N_0 and α:

Case A.—We assume that the IR spectra below $\epsilon_{IR} < 10^{-6}$ (or equivalently, below 1.23×10^{14} Hz) are optically thick for synchrotron self-absorption and adopt $\alpha = 1.5$. Setting $F_\nu = 3$ mJy at $\epsilon_{IR} = 10^{-6}$, which is consistent with near-IR and optical observations (Eikenberry et al. 1997), we obtain $N_0 = 2.3 \times 10^{32}\,\mathrm{cm}^{-3}$.

Case B.—Interpolating the phase-averaged color spectrum in UV, *U*, *B*, *V*, *R* (Percival et al. 1993), *J*, *H*, *K* (Eikenberry et al. 1997) bands, and the radio observation at 8.4 GHz (Moffett & Hankins 1996), we obtain $N_0 = 1.5 \times 10^{17}\,\mathrm{cm}^{-3}$ and $\alpha = -0.88$. In Figure 1, we present the fitted spectrum with the solid line; the ordinate is νF_ν in Jy Hz.

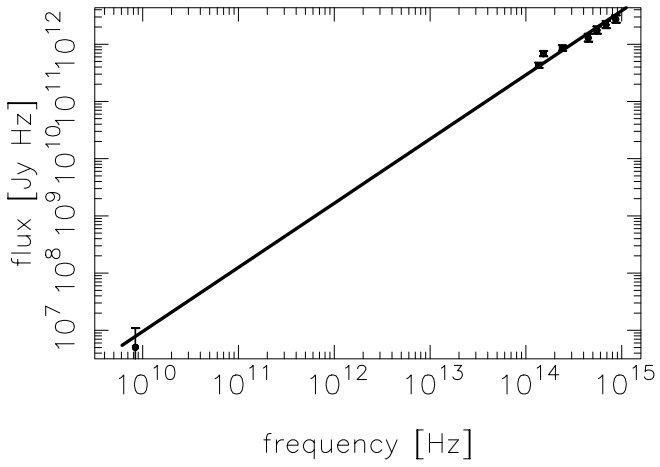

FIG. 1.—Single power-law fit of phase-averaged color spectrum of the Crab pulsar (case B, see § 5.1). The abscissa is the photon frequency in Hz, while the ordinate is the photon flux in Jy Hz.

5.2. *Input X-Ray Field*

HEAO 1 observations revealed that the X-ray spectrum in the primary pulse phase is expressed by

$$\frac{dN_{\rm pl}}{d\epsilon_{\rm x}} = N_{\rm pl}\epsilon_{\rm x}^{\alpha} \quad (\epsilon_{\rm min} < \epsilon_{\rm x} < \epsilon_{\rm max}) , \tag{67}$$

with $\alpha = -1.81$ and $N_{\rm pl} = 5.3 \times 10^{15}(d/{\rm kpc})^2(r_{\rm cnt}/\varpi_{\rm LC})^{-2}$ (Knight 1982). We adopt $\epsilon_{\rm min} = 0.1$ keV/511 keV and $\epsilon_{\rm max} = 50$ keV/511 keV. Unlike the IR field, which is assumed to be homogeneous within radius $\varpi_{\rm LC}$, we suppose that the X-rays are emitted near to the gap. In this case, the X-ray density computed from the observed flux will increase as the gap is located close to the star. To consider such effects, we simply assume that the X-ray density is proportional to the inverse square of $r_{\rm cnt}$.

The angle dependence of the specific intensity of the X-ray field is considered in the collision angle, $\mu_{\rm c}$ (eq. [8], or [40]). In the case of the Crab pulsar, the X-ray field is dominated by a power-law component, which is probably emitted near the outer gap accelerator rather than from the neutron star surface. We thus simply evaluate the cosine of the collision angles as

$$\mu_{\rm c} = \cos\,(W/\varpi_{\rm LC}) \tag{68}$$

for both inwardly and outwardly propagating γ-rays. Aberration of light is not important for this component because both the X-rays and the γ-rays are emitted nearly at the same place. We may notice here that this is a rough estimate of $\mu_{\rm c}$ and that $\epsilon_{\rm th} = 2/[(1-\mu_{\rm c})\epsilon_\gamma]$ strongly depends on $\mu_{\rm c}$ if $W \ll \varpi_{\rm LC}$ (i.e., if $1-\mu_{\rm c} \ll 1$). In the case of the Crab pulsar, $W/\varpi_{\rm LC} \sim 0.05$ holds (see Fig. 2); therefore, the true results will depend on the detailed beaming geometry of the secondary X-rays, which are emitted outside of the gap along local magnetic field lines via the synchrotron process. However, to inquire into this matter would lead us to into that specialized area of the magnetic field configuration close to the light cylinder. Such a digression would undoubtedly obscure the outline of our argument.

5.3. *Results*

Let us now substitute the X-ray field into equation (8) and solve the Vlasov equations by the method described in § 2. It should be noted that we do not use the IR spectrum considered in § 5.1 to solve $E_\parallel(\xi)$, $n_\pm(\xi)$, and $g_\pm{}^i(\xi)$; they are necessary when we consider the TeV emission caused by inverse Compton scatterings.

In Paper I, it is argued that the inverse Compton scatterings dominate the curvature radiation in the outer gap in the Crab pulsar magnetosphere if we adopt $\mu_{\rm c} = 0$. However, in the present paper, we consider that the collision angles are much smaller than 90° and adopt $\mu_{\rm c} = \cos\,(W/\varpi_{\rm LC})$. In this case, unless the gap is located well inside of the conventional null surface, curvature radiation becomes the primary process in γ-ray emission and, hence, in the radiation-reaction forces. The rotational frequency and the magnetic moment are $\Omega = 188.1$ rad s^{-1} and $\mu_{\rm m} = 3.38 \times 10^{30}$ G cm^3.

5.3.1. *Electric Field Structure*

To reveal the spatial distribution of the acceleration field, we consider four representative boundary conditions:

Case 1. $(j_1, j_2) = (0, 0) \rightarrow$ solid curves.
Case 2. $(j_1, j_2) = (0.3, 0) \rightarrow$ dashed curves.
Case 3. $(j_1, j_2) = (0.6, 0) \rightarrow$ dash-dotted curves.
Case 4. $(j_1, j_2) = (0, 0.3) \rightarrow$ dotted curves.

That is, for case 2 (or case 4), the positronic (or electronic) current density flowing into the gap per unit flux tube at the inner (or outer) boundary is 30% of the typical Goldreich-Julian value, $\Omega/2\pi$. We fix $j_{\rm gap} = 0.01$ for all four cases because the solution forms a "brim" and ceases to exist (Fig. 2 in Hirotani & Okamoto 1998) if $j_{\rm gap}$ exceeds a few percent. In what follows, we adopt 45° as the magnetic inclination, which is necessary to compute B at each point for the Newtonian dipole field. Since the X-ray field is dominated by a power-law component, the inclination does not affect $\mu_{\rm c}$.

The results of $E_\parallel(\xi)$ for the four cases are presented in Figure 2. The abscissa designates the distance along the last-open field line and covers the range from the neutron star surface ($s = 0$) to the position where the distance equals $s = 1.2\varpi_{\rm LC} = 1.91 \times 10^6$ m.

The solid curve (case 1) shows that the gap is located around the conventional null surface. However, the gap shifts outward as j_1 increases, as the dashed (case 2) and dash-dotted (case 3) curves indicate.

On the other hand, when j_2 increases, the gap shifts inward and the potential drop, $\Psi(s_2)$, reduces significantly. For example, we obtain $\Psi(s_2) = 7.1 \times 10^{12}$ V for case 4, whereas 1.7×10^{13} V for case 2. A detailed physical interpretation is given in § 6.1.

5.3.2. *Gamma-Ray Spectra*

We compute the GeV and TeV spectrum by the method described in § 4. We adopt the cross-sectional area of $D_\perp{}^2 = (6W)^2$ for all the cases to be considered so that the GeV flux in cases 1 and 2 may be consistent with observations. If $D_\perp$ increases twice, both the GeV and TeV fluxes increase four times.

First, we consider case A, in which the IR spectrum is approximated by synchrotron self-absorption (SSA) with turnover frequency $\sim 1.2 \times 10^{14}$ Hz. In this case, the

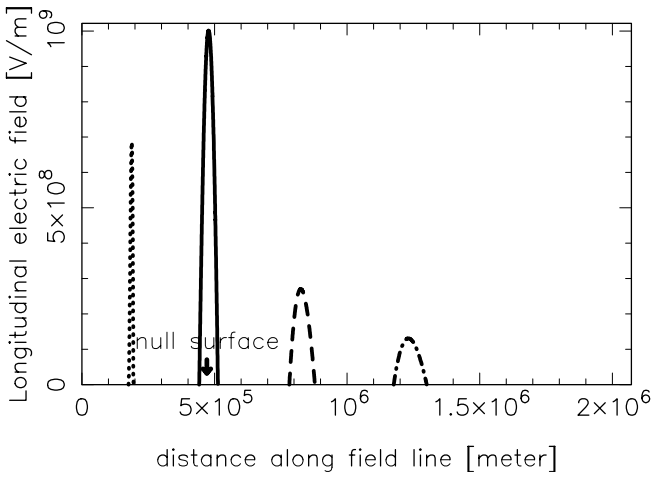

FIG. 2.—Distribution of $E_\parallel(s)$ for the Crab pulsar with $\alpha_{\rm i} = 45°$; the abscissa is in meters. The solid, dashed, dash-dotted, and dotted curves correspond to cases 1, 2, 3, and 4, respectively (see text).

pair-production optical depth τ computed from equation (63) becomes as presented in Figure 3. This result indicates that the TeV flux is significantly absorbed above 1 TeV.

For the four different boundary conditions (cases 1, 2, 3, and 4), we present the spectra of the outwardly and inwardly propagating γ-rays in Figures 4 and 5, respectively. In GeV energies, the observational pulsed spectrum is obtained by EGRET observations (*open circles*; Nolan et al. 1993), while in TeV energies, only the upper limits are obtained by Whipple observations (*open squares*; Weekes et al. 1989; Reynolds et al. 1993; Goret et al. 1993; Hillas et al. 1998; Lessard et al. 2000), Durham observations (*open triangles*; Dowthwaite et al. 1984), and CELESTE observations (*open square* at 60 GeV; J. Holder 2001, private communication). The filled circles denote the unpulsed flux obtained by CANGAROO observations (Tanimori et al. 1998).

It follows from Figures 4 and 5 that the TeV flux is undetectable except for $h\nu \sim 10$ TeV. Around 10 TeV, the γ-ray flux is slightly less than or comparable with the observational upper limits for cases 1, 2, and 3 and exceeds the limits for case 4. Nevertheless, we can exclude case 4 from consideration because the expected GeV spectrum is very very soft and is inconsistent with the EGRET observations, whatever $D_\perp$ we may assume.

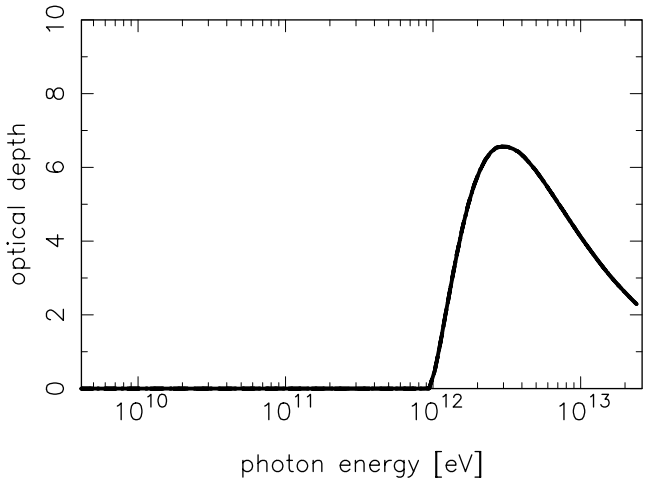

FIG. 3.—Pair-production optical depth for the IR field represented by SSA spectrum (case A).

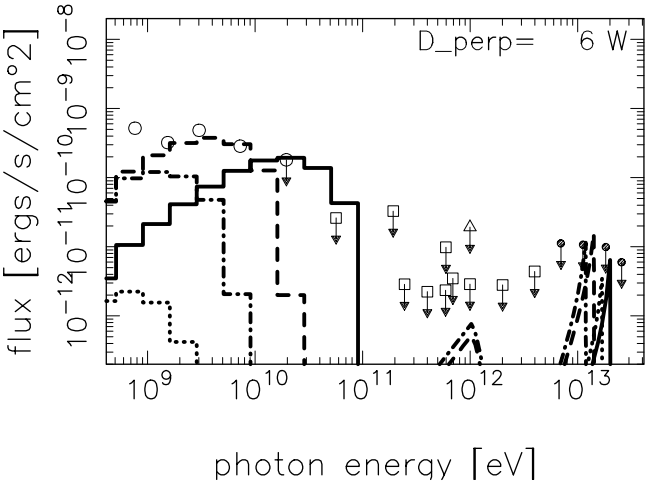

FIG. 4.—Spectra of the outwardly propagating γ-rays emitted from the Crab pulsar magnetosphere when the IR field is approximated by a SSA spectrum (case A). The solid, dashed, dash-dotted, and dotted curves correspond to the same boundary conditions as in Fig. 2.

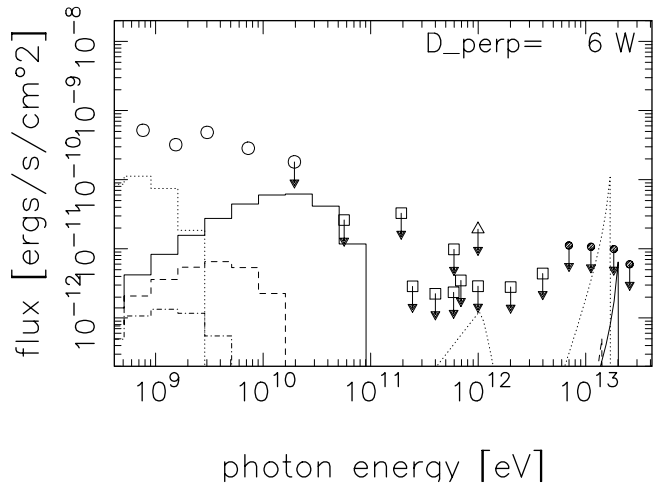

FIG. 5.—Same as Fig. 4 but the γ-rays are inwardly propagating

It is noteworthy that the GeV spectrum, which does not depend on the assumed IR field, depends on j_1 and j_2 significantly. In particular, in case 4 (as the dotted curves show), the GeV emission significantly decreases and softens because both the potential drop and the maximum of $E_\parallel$ reduce as the gap shifts inward. As a result, it becomes impossible to explain the EGRET flux around 10 GeV if the gap is located well inside of the conventional null surface.

Next, let us next consider case B, in which the IR spectrum is interpolated from radio and optical pulsed fluxes. In this case, the pair-production optical depth τ computed from equation (63) becomes as presented in Figure 6. Therefore, the emitted TeV flux significantly reduces above 1 TeV.

The spectra of the outwardly and inwardly propagating γ-rays are presented in Figures 7 and 8, respectively. It follows from the two figures that the TeV fluxes exceed the observational upper limits for cases 2, 3, and 4. In case 1, the

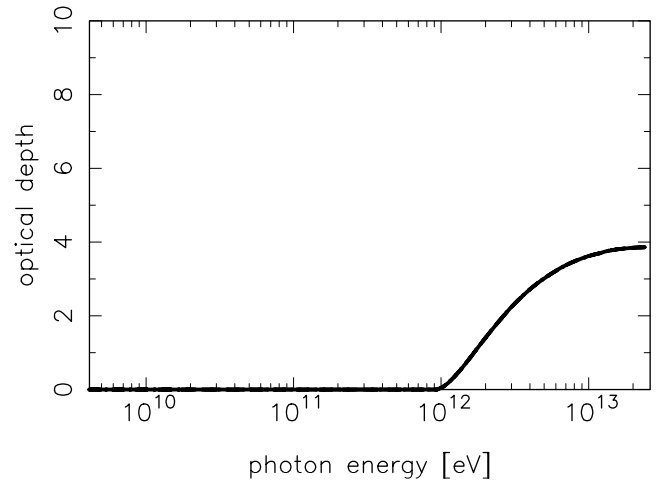

FIG. 6.—Pair-production optical depth for the single power-law IR spectrum (Fig. 1) fitted between radio and optical bands (case B).

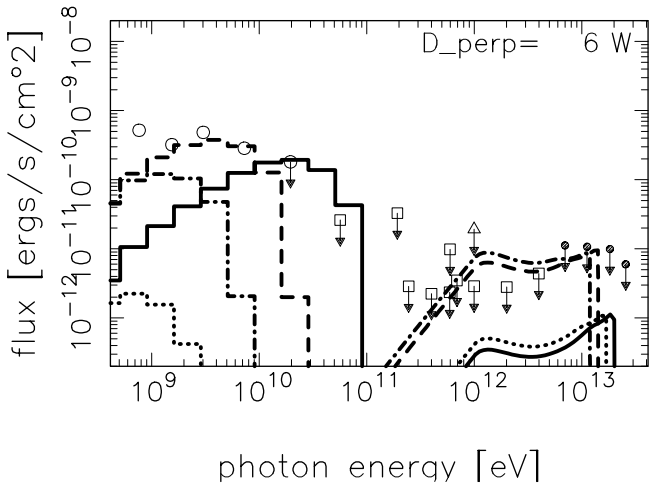

FIG. 7.—Spectra of outwardly propagating γ-rays from the Crab pulsar magnetosphere when the IR spectrum is interpolated from radio and optical bands with a single power law (case B). Solid, dashed, dash-dotted, and dotted curves correspond to the same cases as in Fig. 2.

upscattered flux is small because of its small N_e, which is proportional to $j_{tot} = 0.01$.

Let us briefly consider the case when the interpolated spectrum ($N_0 = 1.5 \times 10^{17}$ and $\alpha = -0.88$) extends to much higher frequencies and adopt $\epsilon_{IR,\,max} = 10^{-5}$ (or 1.2×10^{15} Hz). In this case, $\tau > 2$ holds above 0.2 TeV (Fig. 9); the absorbed TeV flux is thus suppressed below the observational upper limits as Figure 10 indicates.

In short, we can conclude that the problem of the excessive TeV flux does not arise if the IR field is represented by an SSA spectrum (case A) or if the IR field is interpolated by a single power law (case B) with a large cutoff energy ($\epsilon_{IR,max} \sim 10^{-5}$).

5.4. *Dependence on Magnetic Inclination*

To investigate how the results depend on the magnetic inclination, we present the expected Crab pulsar spectra for $\alpha_i = 75°$ in Figure 11. The dashed and dash-dotted curves correspond to cases 2 and 3, while the dash-dot-dot-dotted ones correspond to the case of $j_1 = 0.5$ and $j_2 = 0$. Case 1 is

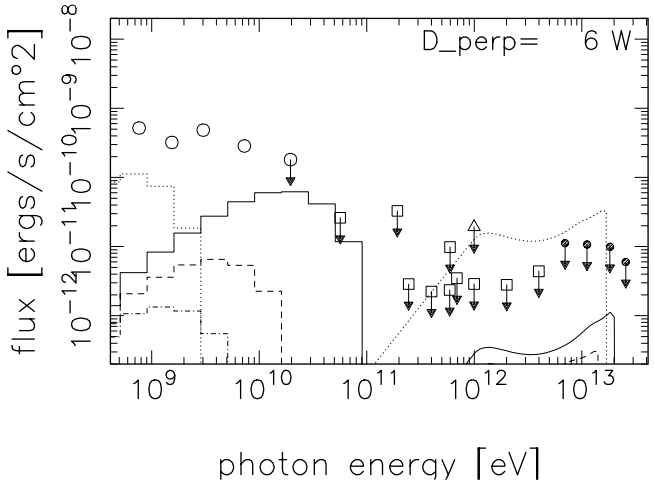

FIG. 8.—Same as Fig. 6 for the Crab pulsar with $\alpha_i = 45°$ but the γ-rays are inwardly propagating.

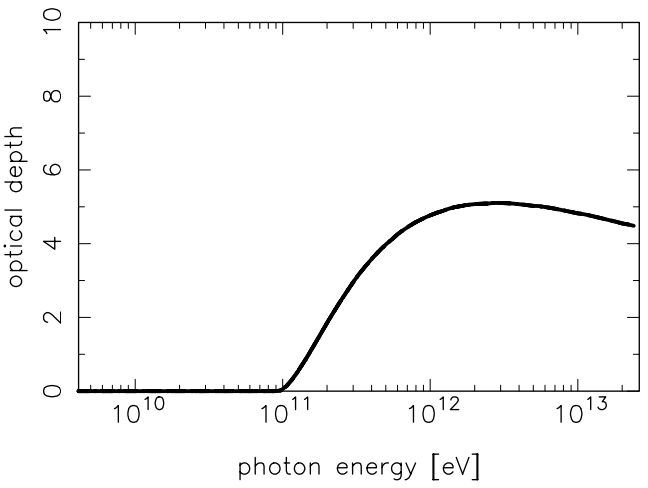

FIG. 9.—Same as Fig. 6 but with a large upper cutoff energy, $\epsilon_{IR,\,max} = 10^{-5}$.

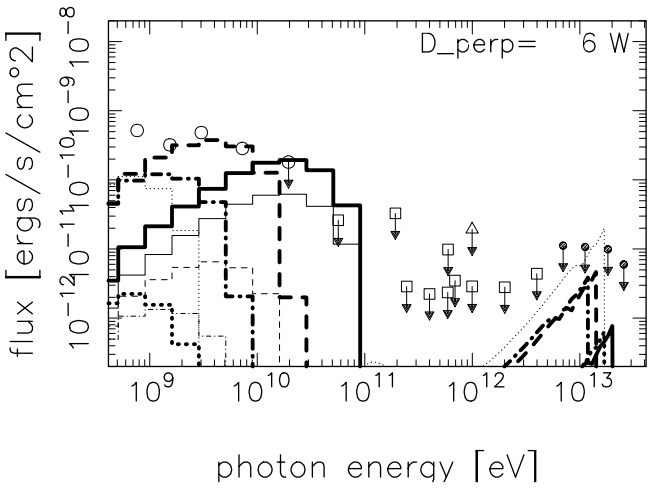

FIG. 10.—Gamma-ray spectra from the Crab pulsar magnetosphere for case B but with a large upper cutoff energy, $\epsilon_{IR,\,max} = 10^{-5}$. Thick (or thin) curves denote outwardly (or inwardly) propagating γ-rays.

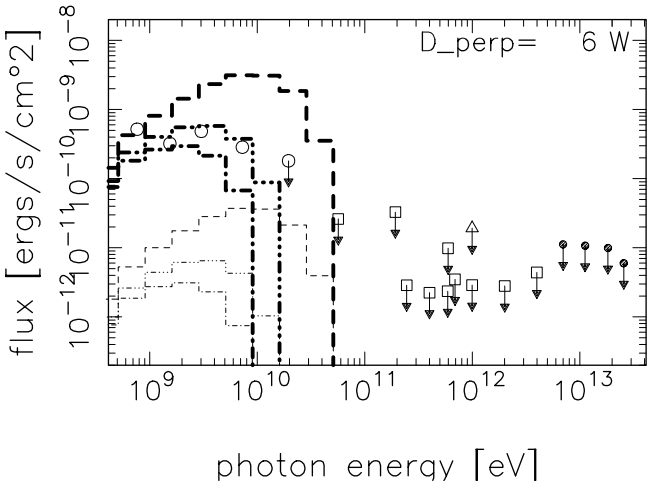

FIG. 11.—Gamma-ray spectra from the Crab pulsar magnetosphere with $\alpha_i = 75°$, when the IR field is approximated by an SSA spectrum (case A). Thick (or thin) curves denote outwardly (or inwardly) propagating γ-rays.

not depicted because the central energy of curvature-radiated photons becomes comparable with $\beta_{11} m_e c^2 = 90.8$ GeV; in this case, its hard spectrum would be inconsistent with the EGRET pulsed spectrum below 30 GeV and the CELESTE upper limit at 60 GeV. Moreover, case 4 (i.e., $j_1 = 0$ and $j_2 = 0.3$) is excluded in Figure 11; this is because the gap is located so close to the star surface that the inverse Compton scatterings dominate the curvature process.

Comparing the GeV spectra in Figure 11 with those in Figures 4 and 5, we can confirm that the curvature emission becomes hard and luminous if α_i increases. Its physical interpretation will be discussed in § 6.2. In Figure 11, case A is adopted as the infrared spectrum; however, the IR field is not important when we discuss the curvature-radiated γ-ray spectrum.

It also follows from Figure 11 that the observed, pulsed GeV spectrum can be explained if we take $j_1 = 0.5$ and $j_2 = 0$ for $\alpha_i = 75°$. In other words, the curvature spectrum becomes analogous between $j_1 = 0.3$ for $\alpha_i = 45°$ (dashed curve in Fig. 4) and $j_1 = 0.5$ for $\alpha_i = 75°$ (thick, dash-dot-dot-dotted one in Fig. 11), if we fix $j_{gap} = 0.01$ and $j_2 = 0$. That is, a greater j_1 is preferable for a greater α_i. It is natural, because the decrease of the distance of the intersection between the conventional null surface and the last-open field line from the star surface (with increasing α_i) should be compensated by shifting the gap outward (with increasing j_1) so that the gap may have the comparable magnetic and X-ray field strengths.

On these grounds, we can conclude that we cannot decouple the effects of the magnetospheric currents (j_1, j_2) and α_i, if we compare only the fluxes of the outwardly propagating γ-rays (when $j_1 > j_2$). It would be possible to argue that these two effects could be decoupled if we considered the inward/outward flux ratio or the three-dimensional structure of the accelerator. However, such details are not pertinent to the main subject of this paper.

6. DISCUSSION

In summary, we have developed a one-dimensional model for an outer gap accelerator in the magnetosphere of a rotation-powered pulsar. When a magnetospheric current flows into the gap from the outer (or inner) boundary, the gap shifts inward (or outward). In particular, when a good fraction of the Goldreich-Julian current density is injected from the outer boundary, the gap is located well inside of the conventional null surface; the resultant GeV emission becomes very soft and weak. Applying this method to the Crab pulsar, we find that the gap should be located near to or outside of the conventional null surface so that the observed GeV spectrum of pulsed GeV fluxes may be emitted via a curvature process. By virtue of the absorption by the dense IR field in the magnetosphere, the problem of excessive TeV emission does not arise.

6.1. *Gap Width versus Current Injection*

By utilizing the gap closure condition (20), we can interpret why W becomes significantly smaller when the gap is located well inside of the conventional null surface (§ 5.3.1). First, the X-ray density becomes large at small radii to reduce λ_p in equation (20). Second, the ratio j_{gap}/j_{tot} decreases as j_2 increases. As a result, W decreases very rapidly with increasing j_2. When W decreases, N_γ decreases to some extent; however, this effect is passive and cannot change the conclusion. On these grounds, the gap width significantly decreases when particles are injected at the *outer* boundary. Therefore, the potential drop also decreases significantly.

On the other hand, when the gap is located outside of the conventional null surface, the decreased j_{gap}/j_{tot} caused by the increase of j_1 partially cancels with the increase of λ_p because of the diluted X-ray field. Thus, the gap width is roughly unchanged when particles are injected at the *inner* boundary.

6.2. *Interpretation of the Magnetic-Inclination Dependence*

In this subsection, we interpret the dependence of the results on α_i (in § 5.4). In Paper V, it was predicted that W ($= 2H$ in their notation) is a decreasing function of α_i for all 12 pulsars considered. The reasons are fivefold:

1. With no current injection (i.e., $j_1 = j_2 = 0$ as considered in Paper V), the gap is located at the intersection of the last-open field line and the conventional null surface, where B_z vanishes.
2. The intersection approaches the star if α_i increases.
3. The density of the X-ray field illuminating the gap increases as the intersection approaches the star (or, equivalently, as r_{cnt} decreases).
4. It follows from the closure condition (eq. [20]) that $W \propto \lambda_p/N_\gamma$. If we neglect the variations in N_γ, W is proportional to $\lambda_p \propto N_x^{-1} \propto r_{cnt}^{-2}$, where N_x is the X-ray number density. Therefore, W decreases with decreasing r_{cnt} and, hence, with increasing α_i.
5. In reality, N_γ decreases if W decreases. As a result of this "negative feedback effect," the decrease of W for an increasing α_i is partially canceled. However, this effect is passive; therefore, the conclusion of the decreasing W with increasing α_i is unchanged.

In Paper V, the GeV emission is predicted to become hard and luminous as α_i increases for the same set of j_{gap}, j_1, and j_2. The reasons are fivefold:

1. The gap approaches the star (i.e., r_{cnt} decreases) as α_i increases for fixed j_1 and j_2 (say, $j_1 = j_2 = 0$ as considered in Paper V).
2. The magnetic field in the gap increases as $B \propto r_{cnt}^{-3}$ when the gap approaches the star.
3. As a result of this rapid increase of B, $E_\parallel$ increases (e.g., eq. [29]), despite the decreasing W, as stated in the paragraph just above.
4. The increased $E_\parallel$ for a larger α_i results in a harder curvature spectrum in GeV energies.
5. The potential drop in the gap is roughly proportional to the maximum of $E_\parallel$ in the gap times W. Because of the "negative feedback effect" caused by N_γ, the weakly decreasing W cannot cancel the increase of $E_\parallel$. As a result, the potential drop and, hence, the GeV luminosity increase with increasing α_i.

6.3. *Super Goldreich-Julian Current*

In this subsection, we briefly discuss the relaxation of the limit of the current density flowing in the gap along the field lines. In Papers I, II, III, VI, in which $j_1 = j_2 = 0$ is assumed, stationary gap solutions were found only for a small j_{gap}. By the revised method presented in this paper, the solutions for the Crab pulsar exist for $j_{gap} < 0.0255$, if we set $j_1 = j_2 = 0$.

The solution of $E_{\parallel}(s)$ for $j_1 = j_2 = 0$ and $j_{\rm gap} = 0.0255$ for the Crab pulsar when $\alpha_{\rm i} = 45^\circ$ is depicted in Figure 12. Because of the "brim" at the inner boundary, no solution exists for $j_{\rm gap} > 0.0255$. In this case, $j_{\rm tot} = j_{\rm gap} + j_1 + j_2$ is limited only below 0.0255, which is much less than the typical Goldreich-Julian value, 1.

Let us briefly consider how much $j_{\rm tot}$ is needed for the observed spin-down luminosity to be emitted. If we assume that all the current flowing in the magnetosphere penetrate the gap, then the net current becomes $J = (\Omega/2\pi) j_{\rm tot} \Psi$, where Ψ is the magnetic flux along which the current is flowing. Assuming a magnetic dipole radiation, we obtain the potential drop at the stellar surface as $V_* \sim \Omega\Psi/(\pi c)$. The spin-down luminosity then becomes

$$\dot{E}_{\rm rot} = J \times V_* \sim \frac{j_{\rm tot}}{c} \left(\frac{\Omega}{\pi} \Psi \right)^2 . \tag{69}$$

If the gap is geometrically thick in the transfield directions, we may expect that the field lines thread the polar cap with area $A_{\rm pole} \equiv \pi (r_* \sin \theta_*)^2$, where r_* refers to the stellar radius and θ_* to the colatitude angle between the magnetic axis and the last-open field line. Utilizing $\sin^2 \theta_*/r_* =$ constant $\sim \Omega/c$ for a dipole geometry, we obtain

$$\Psi \sim \frac{\mu_{\rm m}}{r_*^3} A_{\rm pole} \sim \pi \frac{\Omega \mu_{\rm m}}{c} , \tag{70}$$

where $\mu_{\rm m}$ is the neutron star's magnetic dipole moment. Substituting equation (70) into (69), we obtain

$$\dot{E}_{\rm rot} \sim j_{\rm tot} \frac{\Omega^4 \mu_{\rm m}^2}{c^3} . \tag{71}$$

For the Crab pulsar, $\Omega^4 \mu_{\rm m}^2/c^3 = 10^{38.6}$ ergs s^{-1}; therefore, $j_{\rm tot} \sim 1$ is required so that the observed spin-down luminosity $10^{38.65}$ ergs s^{-1} may be realized. Analogous conclusions are derived for other rotation-powered pulsars. Moreover, the sharp pulse of the Crab pulsar may imply $A_{\rm pole} \ll \pi (r_* \sin \theta_*)^2$; therefore, even $j_{\rm gap} \gg 1$ may be required. On these grounds, the limitation of $j_{\rm tot} = j_{\rm gap} \ll 1$ derived for $j_1 = j_2 = 0$ was insufficient to apply to realistic pulsars.

In this paper, we relaxed the limitation of $j_{\rm tot}$ by allowing j_1 or j_2 to be nonvanishing. The results of the predicted

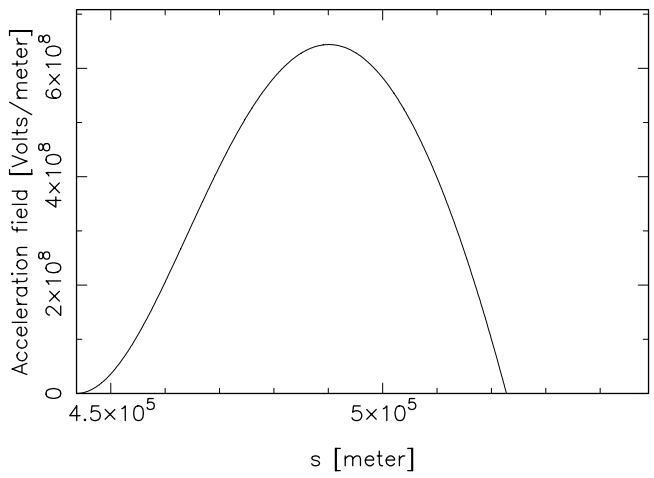

FIG. 12.—Distribution of $E_{\parallel}(s)$ for the Crab pulsar with $\alpha_{\rm i} = 45^\circ$ when $j_{\rm gap} = 0.0255, j_1 = j_2 = 0$.

γ-ray spectra are, therefore, more realistic as compared with previous results obtained in Papers I, II, III, VI. However, even in this treatment, $j_{\rm tot}$ is limited below unity.

The next issue, therefore, is to consider whether we can construct an outer gap model with super–Goldreich-Julian current density (i.e., $j_{\rm gap} > 1$). The Poisson equation (30) tells us that solutions exist even for $j_1 + j_2 \gg 1$, provided that $j_1 - j_2 < 1$. (For example, if $j_1 = j_2 \gg 1$, the gap exists at the conventional null surface.) In this case, W becomes much smaller than those obtained for $j_1 + j_2 < 1$ because of the gap closure condition (eq. [20]). In the case of the Crab pulsar, the small W obtained for $j_1 + j_2 > 1$ fails the mono-energetic approximation. To find solutions for $j_{\rm tot} \sim j_1 + j_2 \gg 1$, we could assume much smaller collision angles so that the pair-production mean free path may become much larger. To settle this issue, we must constrain the magnetic field geometry around the gap and quantitatively infer the collision angles between the primary γ-rays and the secondary X-rays.

In short, stationary gap solutions exist even for a super–Goldreich-Julian current. In this case, the collision angles should be much less than $W/\varpi_{\rm LC}$ so that the emitted γ-ray flux may be consistent with observations for the young pulsars for which the X-ray field is dense (like Crab). For older pulsars with X-ray fields that are less dense, on the other hand, we can in fact find solutions with super–Goldreich-Julian current. This will be discussed in a subsequent paper.

6.4. *Comparison with Previous Works*

Let us compare the present methods and results with Paper V. In this paper, $E_{\parallel}$, $N_{\pm}(s)$, and $G_{\pm}(s, \epsilon_\gamma)$ were solved from the Vlasov equations for a nonvacuum gap, while in Paper V only $E_{\parallel}$ field was solved from the Poisson equation for a vacuum gap, with the aid of W, which was deduced from the gap closure condition. In the stationary gap, the Vlasov equations automatically satisfy the closure condition; therefore, the obtained electrodynamic structures (e.g., W, $E_{\parallel}$) are essentially the same between the two papers, provided that the gap is nearly vacuum (i.e., $j_{\rm tot} \ll 1$). By relaxing the boundary conditions of the magnetospheric current, and by solving the nonvacuum solution from the Vlasov equations, we first find in this paper an interesting behavior of the gap position: The gap shifts outward (or inward) when current is injected from the inner (or outer) boundary. The obtained GeV spectra are similar between the two papers, unless the gap is located well inside of the conventional null surface. In Paper V, the intrinsic TeV spectra were depicted in Figure 6; on the other hand, in this paper, the TeV spectra after absorption were depicted in Figures 4, 5, 7, 8, and 10.

We briefly compare the present method with ZC97, who considered that the gap width is limited by the surface X-rays caused by the bombardment of the particles produced in the gap. The magnetospheric X-rays considered in this paper are much denser than the surface X-rays caused by the bombardment. As a result, the localized gap in the present paper produces less intrinsic TeV flux compared with what would be obtained in the ZC97 picture.

6.5. *Possibility of Another Solution Branch*

For cases 1, 2, and 3, the intrinsic TeV luminosity is comparable or less than the GeV one. Therefore, the

Lorentz factors are limited primarily by the curvature process (eq. [45]). For case 4, however, the intrinsic TeV luminosity well exceeds the GeV one; therefore, the radiation-reaction forces are caused by inverse Compton scatterings rather than the curvature process. In fact, we may expect a sufficient GeV flux via inverse Compton scatterings when the gap is located well inside of the conventional null surface. This is because the dense X-ray field will suppress the particle Lorentz factors (Paper II) and because the less-energetic particles scatter copious IR photons into lower γ-ray energies with large cross sections ($\sim\sigma_T$). There is room for further investigation on this issue.

K. H. wishes to express his gratitude to Y. Saito and A. K. Harding for valuable advice. He also thanks the Astronomical Data Analysis Center of National Astronomical Observatory, Japan, for the use of workstations.

REFERENCES

Akerlof, C. W., et al. 1993, A&A, 274, L17
Blumenthal, G. R., & Gould, R. J. 1970, Rev. Mod. Phys., 42, 237
Borione, A., et al. 1997, ApJ, 481, 313
Cheng, K. S., Ho, C., & Ruderman, M. 1986a, ApJ, 300, 500
———. 1986b, ApJ, 300, 522
Chiang, J., & Romani, R. W. 1992, ApJ, 400, 629
———. 1994, ApJ, 436, 754
Daugherty, J. K., & Harding, A. K. 1982, ApJ, 252, 337
———. 1996, ApJ, 458, 278
Dowthwaite, J. C., et al. 1984, ApJ, 286, L35
Eikenberry, S. S., Fazio, G. G., Ransom, S. M., Middleditch, J., Kristaian, J., & Pennypacker, C. R. 1997, ApJ, 477, 465
Goret, P., Palfey, T., Tabary, A., Vacanti, G., & Bazen-Bachi, R. 1993, A&A, 270, 401
Harding, A. K., Tademaru, E., & Esposito, L. S. 1978, ApJ, 225, 226
Fierro, J. M., Michelson, P. F., Nolan, P. L., & Thompson, D. J. 1998, ApJ, 494, 734
Hillas, A. M., et al. 1998, ApJ, 503, 744
Hirotani, K. 2000a, MNRAS, 317, 225 (Paper IV)
———. 2001, ApJ, 549, 495 (Paper V)
———. 2000b, PASJ, 52, 645 (Paper VI)
Hirotani, K., & Okamoto, I. 1998, ApJ, 497, 563
Hirotani, K., & Shibata, S. 1999a, MNRAS, 308, 54 (Paper I)
———. 1999b, MNRAS, 308, 67 (Paper II)
———. 1999c, PASJ, 51, 683 (Paper III)
Knight F. K. 1982, ApJ, 260, 538
Krause-Polstorff, J., & Michel, F. C. 1985a, MNRAS, 213, 43
———. 1985b, A&A, 144, 72
Lessard, R. W., et al. 2000, ApJ, 531, 942
Michel, F. C. 1974, ApJ, 192, 713
———. 1991, ApJ, 383, 808
Moffett, D. A., & Hankins, T. H. 1996, ApJ, 468, 779
Nel, H. I., De Jager, O. C., Raubenheimer, B. C., Brink, C., Meintjes, P. J., & Nortt, A. R. 1993, ApJ, 418, 836
Nolan, P. L., et al. 1993, ApJ, 409, 697
Percival, J. W., et al. 1993, ApJ, 407, 276
Reynolds, P.T., et al. 1993, ApJ, 404, 206
Romani, R. W. 1996, ApJ, 470, 469
Romani, R. W., & Yadigaroglu, I. A. 1995, ApJ, 438, 314
Rybicki, G. B., & Lightman, A. P. 1979, Radiative Processes in Astrophysics (New York: Wiley)
Sako, T., et al. 2000, ApJ, 537, 422
Shibata, S., Miyazaki, J., & Takahara, F. 1998, MNRAS, 295, L53
Srinivasan, R., et al. 1997, ApJ, 489, 170
Sturner, S. J., Dermer, C. D., & Michel, F. C. 1995, ApJ, 445, 736
Tanimori, T., et al. 1998, ApJ, 492, L33
Usov, V. V. 1994, ApJ, 427, 394
Weekes, T. C., et al. 1989, ApJ, 342, 379
Yoshikoshi, T., Kifune, T., Dazeley, S. A., Edwards, P. G., Hara, T., Hayami, Y., Kakimoto, F., & Konishi, T. 1997, ApJ, 487, L65
Zhang, L., & Cheng, K. S. 1997, ApJ, 487, 370 (ZC97)